2',3' cyclic-nucleotide 3'-phosphodiesterase (CNP) inhibits SARS-CoV-2 virion assembly by blocking infection-induced mitochondria depolarization

James Logue[1,2], Victoria M. Melville[1,2], Jeremy Ardanuy[1,2], Matthew B. Frieman[1,2,#]

[1]The Department of Microbiology and Immunology, The University of Maryland School of Medicine, Baltimore, MD, 21201.

[2]Center for Pathogen Research, The University of Maryland School of Medicine, Baltimore, MD, 21201.

[#]Correspondence: M.B.F (mfrieman@som.umaryland.edu)

Abstract

The COVID-19 pandemic has claimed over 6.5 million lives worldwide and continues to have lasting impacts on the world's healthcare and economic systems. Several approved and emergency authorized therapeutics that inhibit early stages of the virus replication cycle have been developed however, effective late-stage therapeutical targets have yet to be identified. To that end, our lab identified 2',3' cyclic-nucleotide 3'-phosphodiesterase (CNP) as a late-stage inhibitor of SARS-CoV-2 replication. We show that CNP inhibits the generation of new SARS-CoV-2 virions, reducing intracellular titers by over 10-fold without inhibiting viral structural protein translation. Additionally, we show that targeting of CNP to mitochondria is necessary for inhibition, implicating CNP's proposed role as an inhibitor of the mitochondrial permeabilization transition pore as the mechanism of virion assembly inhibition. We also demonstrate that adenovirus transduction of a dually over-expressing virus expressing human ACE2, in cis with either CNP or eGFP inhibits SARS-CoV-2 titers to undetectable levels in lungs of mice. Collectively, this work shows the potential of CNP to be a new SARS-CoV-2 antiviral target.

Introduction

Severe acute respiratory syndrome coronavirus 2 (SARS-CoV-2) is the etiologic agent of coronavirus disease 2019 (COVID-19), first reported in Wuhan City, Hubei Provence, China in December 2019 [1-3]. Since then, SARS-CoV-2 infections have expanded to a worldwide pandemic, with over 675 million reported cases and over 6.8 million reported deaths at the time of writing [4, 5]. In the absence of broad-spectrum, small molecule antiviral treatments, much of the early COVID-19 therapeutic research focused on the potential repurposing of compounds already approved by the United States Food and Drug Administration (FDA) for other diseases [6-8]. Though an overwhelming majority of compounds did not prove effective, a small number were tested in clinical trials, with only the nucleoside analogues Remdesivir and Molnupiravir receiving FDA Emergency Use Authorization or full approval for the treatment of early COVID-19 by the time of writing [9, 10]. In addition to repurposed compounds, SARS-CoV-2-specific therapies have been authorized or approved by the FDA, including the oral protease inhibitor Paxlovid and several monoclonal antibody treatments [11-14].

SARS-CoV-2 infection begins with binding of the surface protein Spike (S) to the cellular receptor, angiotensin converting enzyme II (ACE2), following which S can be cleaved on the cell surface by Transmembrane protease serine 2 (TMPRSS2) or by Cathepsins B or L in endosomes to facilitate membrane fusion and viral genome release into the cytosol [15-21]. Nonstructural proteins are then immediately translated to a polyprotein to be liberated into individual proteins by viral mediated proteolysis, leading to the formation of replication organelles (DMVs) [22-25]. RNA replication then occurs in these organelles, resulting in the generation of new viral genomes and the production of viral subgenomic RNA (sgRNA), the coronavirus equivalent of mRNA, that are translated into structural and accessory proteins [22, 26]. Assembly of new SARS-CoV-2 virions occurs at the ER-Golgi Intermediate Compartment (ERGIC) followed by virus exit by a still undefined exocytotic method [27-29].

Interestingly, all therapeutics currently authorized or approved by the FDA target early stages of the SARS-CoV-2 life cycle (e.g., entry, RNA replication). However, later stages of the SARS-CoV-2 life cycle are relatively not well understood and, consequently, late-stage inhibitors that could prove more effective or work synergistically with early-stage inhibitors are lacking. We previously identified 2’, 3’-

51 cyclic nucleotide 3'-phosphodiesterase (CNP) as a late-lifecycle-stage SARS-CoV-2 inhibitor in an
52 overexpression screen of 399 interferon stimulated genes (ISGs) [30]. CNP is a lipid-bound protein that is
53 expressed throughout the body, including pulmonary tissues, but expressed at very high levels in myelin
54 [31-33]. Though early biochemical studies identified CNP by its ability to hydrolyze 2',3'-cyclic
55 nucleotides, as the name suggests, an exact function and a potential cellular substrate have yet to be
56 demonstrated *in vitro* or *in vivo* [34]. However, a growing pool of evidence has begun to establish
57 potential functions for the mitochondria-targeted isoform of CNP (CNP2), which has been shown to
58 inhibit opening of the mitochondrial permeabilization transition pore (mPTP), a process that leads to
59 mitochondrial depolarization in response to mitochondrial Ca^{2+} overload, cellular oxidative stress, or
60 potentially SARS-CoV-2 infection [35-39]. In our previous work, we showed CNP overexpression
61 inhibited SARS-CoV-2 replication in all the cell lines tested, including primary human tracheobronchial
62 epithelial cells, and further showed the inhibition to occur at a replication lifecycle stage post-genome
63 replication [30]. However, the exact lifecycle stage affected and the mechanism of action has yet to be
64 identified.
65 In this study, we confirm that overexpression of CNP *in vitro* has no effect on SARS-CoV-2
66 genome replication and further show CNP affects neither subgenomic RNA generation nor structural
67 protein translation. However, CNP overexpression reduced SARS-CoV-2 N localization to sites of virion
68 assembly (ERGIC) and reduced intracellular SARS-CoV-2 titers, providing strong evidence that virion
69 assembly is inhibited. Additionally, we show that CNP inhibition of SARS-CoV-2 required mitochondrial
70 targeting of CNP, which reduced SARS-CoV-2-induced mPTP opening and mitochondrial reactive
71 oxygen species (ROS) release. Indeed, replacing reactive oxygen species in CNP stably-expressing cells
72 through peroxide treatment resulted in a rescue of virus titer. Finally, we show that CNP overexpression
73 in Balb/c laboratory mouse lungs protected mice from SARS-CoV-2 infection, reducing lung virus titers
74 by over 1,000-fold. This work highlights the importance of cytosolic ROS for SARS-CoV-2 virion
75 assembly and identifies CNP as a potential therapeutic target for COVID-19.
76

77 # Results

78 **CNP inhibits SARS-CoV-2 virion assembly.**

79 Previous data from our lab shows that CNP overexpression inhibits a SARS-CoV-2 lifecycle
80 stage post-genome replication [30]. To further elucidate the stages affected, HEK293T/hACE2 cells
81 stably expressing HA-tagged CNP or HA-tagged GFP were generated by lentivirus transduction
82 (Supplemental Figure S1). Cells were then infected with SARS-CoV-2/WA1 for a 45-minute absorption
83 period followed by washing with cell culture media to remove any remaining unbound virus. Various
84 assays were then used to assess the effects of CNP overexpression on multiple SARS-CoV-2 lifecycle
85 stages. At 6-hours post-infection (hpi), we confirmed that gRNA levels are not significantly different
86 between CNP stable cells and GFP stable cells (Fig 1a) and, further show that sgRNA levels are not
87 altered by CNP (Fig 1b). At 12hpi, western blots for SARS-CoV-2 structural proteins S and N were also
88 not qualitatively different between CNP and GFP stable cells, suggesting no effect on structural protein
89 translation (Fig 1c). However, at 18hpi, SARS-CoV-2 titers were significantly lower when assessed for
90 both intracellular titer (Fig 1d) and extracellular titer (Fig 1e), suggesting the assembly of new SARS-
91 CoV-2 virions is affected by CNP. As SARS-CoV-2 virion assembly takes place at the ERGIC, infected
92 stable cell lines were then fixed at 12hpi and immunofluorescent stained for ERGIC53 and co-stained
93 with either SARS-CoV-2 S or N. Images were captured by confocal microscopy and colocalization was
94 assessed. HEK293T/hACE2 cells stably expressing CNP showed higher colocalization between ERGIC
95 and SARS-CoV-2 S as compared to GFP control cells (Fig 2a, quantified in Fig 2c). However,
96 colocalization between SARS-CoV-2 N and ERGIC markers was markedly lower for CNP expressing
97 cells as compared to GFP controls (Fig 2b, quantified in Fig 2d), suggesting an inhibition of N trafficking
98 to sites of virion assembly.

99

100 **CNP inhibits SARS-CoV-2-induced mitochondria depolarization.**

101 In order to assess the necessary aspects of CNP required for SARS-CoV-2 inhibition,
102 HEK293T/hACE2 cells were transfected with HA-tagged CNP or HA-tagged CNP mutation/deletion
103 constructs, including constructs with mutations to the known catalytic sites (H251A, T253A, H330A,
104 T332A) and prenylation site (C418A) and deletions of the mitochondrial targeting sequence (Δ1-20)
105 (Supplemental Figure S1, Supplemental Table S2). Other domain deletion constructs (i.e., Δ p-loop
106 domain, Δ catalytic domain) were abandoned due to bad expression, likely caused by protein misfolding
107 (Supplemental Figure S1). The day following transfections, cells were infected with SARS-CoV-2/WA1
108 (MOI = 0.01) for 48 hours, at which point supernatants were collected and SARS-CoV-2 titers
109 determined by plaque assay. As shown previously, CNP overexpression resulted in a greater than 10-fold
110 decrease in SARS-CoV-2 titers as compared to GFP controls. However, deletion of the mitochondrial
111 targeting sequence resulted in ablation of SARS-CoV-2 inhibition, suggesting targeting of CNP to
112 mitochondria is required for antiviral activity (Fig 3a).
113 Given this result, we aimed to assess the effects of CNP overexpression on mitochondrial
114 function during SARS-CoV-2 infection. Previous work has shown that SARS-CoV-2 infection leads to
115 mPTP-induced mitochondrial depolarization as soon as 3hpi [39]. Additionally, others have shown that
116 CNP inhibits the formation and function of the mPTP [36, 37]. To further assess this relationship,
117 HEK293T/hACE2 cells were transfected with hCNP, hCNPΔMTS, or empty plasmid constructs as
118 described above and infected the following day with SARS-CoV-2/WA1 (MOI = 5). At 6hpi, cells were
119 stained with JC10 dye to assess mitochondrial depolarization or TMRM dye to assess mPTP opening. As
120 was shown previously, SARS-CoV-2 infection in control-transfected cells and hCNPΔMTS-transfected
121 cells led to mitochondrial depolarization, as shown by increases in JC10 staining (Fig 3b) and opening of
122 the mPTP as shown by loss of TMRM staining, as compared to mock infected cells. However, these
123 effects were not observed for hCNP-transfected cells, suggesting hCNP inhibits SARS-CoV-2-mediated
124 mitochondrial depolarization. To further assess the effects of hCNP on mPTP function,
125 HEK293T/hACE2 cells stably expressing either hCNP or GFP were infected with SARS-CoV-2 followed
126 by treatment with 10μM Cyclosporin A, an established inhibitor of mPTP function, or DMSO as a vehicle

127 control. Intracellular SARS-CoV-2 titers were significantly lower when Cyclosporin A treatment was
128 administered to GFP stable cells but not lower for hCNP stable cells, as compared to vehicle controls (Fig
129 3d).
130
131 **Mitochondrial reactive oxygen species release is needed for efficient SARS-CoV-2 virion assembly.**
132 We have confirmed that SARS-CoV-2 infection can induce mitochondrial dysfunction and
133 further show that this dysfunction can be inhibited by hCNP. One major consequence of sustained
134 mitochondrial depolarization is the production and release of ROS. To assess the importance of ROS to
135 SARS-CoV-2 virion assembly inhibition, HEK293T/hACE2 cells were transfected with hCNP,
136 hCNPΔMTS, or empty plasmid constructs as described above and infected the following day with SARS-
137 CoV-2/WA1 (MOI = 5). At 6hpi, cells were stained with H_2DCFDA to visualize cytosolic ROS (Fig 4a).
138 As was shown previously, SARS-CoV-2 infection in control-transfected cells and hCNPΔMTS-
139 transfected cells led to increased ROS production, as compared to mock infected cells. However, these
140 effects were not observed for hCNP-transfected cells, suggesting hCNP-inhibition of mitochondrial
141 depolarization may lead to inhibition of ROS production and release into the cytosol.
142 To further confirm the importance of ROS production to SARS-CoV-2 replication, we infected
143 HEK293/hACE2 cells stably expressing either hCNP or GFP with SARS-CoV-2/WA1 (MOI = 5) for a
144 45-minute absorption period followed by washing with cell culture media to remove any remaining
145 unbound virus. At 3hpi, cells were then treated with a sub-lethal concentration range of hydrogen
146 peroxide, one of the ROS released following mitochondrial depolarization, and intracellular/extracellular
147 SARS-CoV-2 titers assessed at 18hpi. The addition of ROS to hCNP-stable HEK293T/hACE2 cells
148 resulted in a dose-dependent rescue of SARS-CoV-2 titers as compared to GFP control cells when
149 assessed for intracellular (Fig 4b) or extracellular (Fig 4c) titers. This data suggests that ROS release from
150 the mitochondria is required for SARS-CoV-2 virion assembly and release.
151
152 **CNP reduces SARS-CoV-2 infection in a mouse model of COVID-19.**

153 To assess the effects of CNP on SARS-CoV-2 infection in a mouse model of COVID-19, rAd5
154 vectors were generated to dually express hACE2, the SARS-CoV-2 entry receptor, and either HA-tagged
155 hCNP or HA-tagged eGFP. To validate rAd5 transduction efficiency, Balb/c laboratory mice were
156 transduced intranasally with 1 x 10^8 viral particles (VP) per mouse and effects on weight change and
157 hCNP and hACE2 expression were assessed 3-days post-transduction (Fig 5a). rAd5 transduction resulted
158 in minimal weight-loss (Fig 5b) by 3-days post-transduction and we observed no qualitative differences in
159 pulmonary inflammation as shown by histology (data not shown). Transduction by either rAd5 vector
160 resulted in increased expression of hACE2 (Fig 5c) and HA-tagged hCNP or HA-tagged eGFP (Fig 5d) as
161 visualized by immunofluorescent staining of lung histology sections. Additionally, levels of hACE2
162 mRNA were elevated due to either rAd5 transduction (Fig 5e) and hCNP mRNA was elevated in
163 rAd5/hCNP transduced animals (Fig 5f).
164 Using these validated rAd5 vectors, we next assessed effects of CNP on SARS-CoV-2 infection
165 in an animal COVID-19 disease model. Balb/c laboratory mice were intranasally transduced with rAd5
166 vectors (1 x 10^8 VP/mouse) 3 days-prior to intranasal challenge with SARS-CoV-2/WA1 (1 x 10^3
167 pfu/mouse or 1 x 10^5 pfu/mouse) (Fig 6a). Importantly, the WA1 strain of SARS-CoV-2 cannot enter
168 cells using murine ACE2 and will only be able to infect rAd5-transduced cells expressing hACE2. hCNP
169 overexpression resulted in a greater than 1000-fold decrease in live virus titers to undetectable levels from
170 mouse lung homogenates at 2- or 4-dpi for either the 1 x 10^3 pfu/mouse (Fig 6b) or 1 x 10^5 pfu/mouse
171 (Fig 6c) challenge groups. Additionally, there was a marked decrease in SARS-CoV-2 sgRNA in lungs
172 from hCNP transduced animals as compared to control animals for either 1 x 10^3 pfu/mouse (Fig 6d) or 1
173 x 10^5 pfu/mouse (Fig 6e) challenge groups.
174

175 ## Discussion

176 Therapeutics against COVID-19 remain limited to early SARS-CoV-2 replication cycle targets,
177 including monoclonal antibody treatments that block entry and nucleoside analogues that inhibit viral

178 RNA replication. This is in part due to the relative gap in understanding that remains for later SARS-
179 CoV-2 lifecycle stages. Our work aimed to further define the mechanism of action of a potential late-
180 stage inhibitor of SARS-CoV-2, CNP, to both assess its therapeutic potential and to further investigate
181 later SARS-CoV-2 lifecycle stages. Consistent with our previously published work, we confirmed that
182 CNP overexpression had no effect on SARS-CoV-2 genome replication but resulted in a significant
183 decrease in extracellular SARS-CoV-2 titers, again suggesting CNP inhibits somewhere between these
184 viral lifecycle steps. We further showed that the generation of sgRNA, the equivalent of the viral mRNA,
185 and translation of SARS-CoV-2 structural proteins were similarly not affected by CNP overexpression.
186 However, intracellular SARS-CoV-2 titers were significantly reduced in CNP overexpressing cells,
187 suggesting the generation of newly made virions is hampered in the presence of CNP. Indeed, CNP
188 overexpression resulted in a reduction of N localization to sites of virion assembly, the ERGIC, and
189 resulted in higher amounts of S localization at the ERGIC, suggesting unincorporated S may be
190 sequestered at the ERGIC awaiting assembly with N. Collectively, these data show that CNP inhibits the
191 assembly of new SARS-CoV-2 virions.

192 Our work also demonstrates the importance of mitochondrial depolarization to efficient virion
193 assembly. SARS-CoV-2 infection has been shown previously to lead to mitochondrial dysfunction and
194 the release of ROS, though no specific connection to viral replication was made [39]. Our study shows
195 that CNP targeting to mitochondria was essential for SARS-CoV-2 inhibition and that this targeting
196 decreased SARS-CoV-2-induced mitochondrial depolarization and ROS release. Interestingly, the
197 catalytic activity of CNP appeared to be somewhat dispensable for SARS-CoV-2 inhibition, suggesting
198 catalytic activity may not be required for mPTP inhibition, as has been suggested previously [36, 37].
199 Additionally, the inhibition of ROS production and release caused by mPTP opening appeared to be
200 driving SARS-CoV-2 inhibition, as the addition of ROS to infected CNP-expressing cells by peroxide
201 treatment rescued SARS-CoV-2 intracellular and extracellular titers. Further research will be needed to
202 assess how ROS release leads to more efficient virion assembly. It is possible that cytosolic ROS may
203 provide a more advantageous environment for post-translational modification to SARS-CoV-2 structural

204 proteins that regulate virion assembly, such as modifications to N that are proposed to regulate N phase
205 separation to promote virion assembly [40]. Alternatively, increases in ROS signaling could promote
206 virion assembly.

207 This study also shows the potential of CNP to be developed into a potent COVID-19 therapeutic.
208 Our mouse data shows that pre-treatment with CNP inhibited SARS-CoV-2 infection to below detectable
209 levels in lungs throughout the course of infection. Additionally, overexpression of CNP when
210 administered intranasally in mice showed no substantial side effects as measured by weight loss or
211 visualized by histology for pulmonary inflammation, suggesting a CNP treatment could be well tolerated.
212 Additionally, increases in systemic ROS during acute COVID-19 has been observed in humans and
213 implicated in the development of some "Long COVID" symptoms [41]. It is possible that CNP treatment
214 could alleviate some of these long-term effects. However, further development is needed to transition a
215 potential CNP treatment from rAd5 transduction to a more viable treatment option. Alternatively, other
216 mPTP inhibitors, such as Cyclosporin A, could show additional promise as a COVID-19 treatment *in vivo*
217 than what has already been demonstrated *in vitro* [39]. Collectively, this work shows the potential of
218 mPTP inhibition and reduction in ROS production as a treatment for COVID-19 and the potential of CNP
219 to be a new SARS-CoV-2 antiviral target.

220

221 # Material and Methods

222 **Cells**

223 VeroE6 cells overexpressing TMPRSS2 were generously provided by Dr. Makoto Takeda
224 (VeroT, [42]). VeroT and HEK293T cells overexpressing hACE2 (HEK293T/hACE2) (ATCC BEI NR-
225 52511) were cultured in DMEM medium (Quality Biological) supplemented with 10% (vol/vol) heat-
226 inactivated FBS (Sigma), 1% (vol/vol) penicillin–streptomycin (Gemini Bio-Products), 1% (vol/vol) l-
227 glutamine (2 mM final concentration; Gibco), and 1% (vol/vol) HEPES buffer (10mM final
228 concentration; Gibco).

229 **Virus**

230 All work with SARS-CoV-2 was performed in an A/BSL3 laboratory and approved by our
231 Institutional Biosafety Committee (IBC# IBC-00005484) and Institutional Animal Care and Use
232 Committee (IACUC# 1120004). The original strain of SARS-CoV-2 was provided by the CDC following
233 isolation from a patient in Washington State (WA-1; BEI number NR-52281). Stocks were prepared by
234 infection of VeroT cells for two days when a cytopathic effect was starting to become visible. The media
235 were collected and clarified by centrifugation before being aliquoted for storage at −80 °C. The titer of the
236 stock was determined by plaque assay using VeroT cells.

237 Lentiviruses and adenoviruses were purchased from and prepared by VectorBuilder Inc. Any
238 infections with lentiviruses and adenoviruses were performed in an A/BSL2 or A/BSL3 laboratory and
239 approved by our Institutional Biosafety Committee (IBC# IBC-00005484) and Institutional Animal Care
240 and Use Committee (IACUC# 1120004).

241 **Semi-solid Avicel Plaque Assay**

242 Plaque assays were performed similar to what has been described previously [43]. Briefly, 12-
243 well plates were seeded with 2.5 x 10^5 VeroT cells/well one day prior to processing. On the day of
244 processing, media was removed from the 12-well plates and 200µL of dilutions of sample in DMEM were
245 added to each well. Plates were incubated at 37 °C (5% CO_2) for 1 hour with rocking every 15 minutes.
246 Following incubation, 2mL of plaque assay media, DMEM containing 0.1% agarose (UltraPure™) and
247 2% FBS (Gibco), was added to each well and incubated for 2 days at 37 °C (5% CO_2). Following
248 incubation, plates were fixed with 4% paraformaldehyde, stained with 0.25% crystal violet (w/v), plaques
249 counted, and titers calculated as plaque forming units (PFU).

250 **RT-qPCR**

251 RT-qPCR was processed for cell lysate and for mouse lung homogenates as described previously
252 [43]. RNA was extracted per the manufacturer's instructions using the Direct-zol RNA Miniprep Kit
253 (Zymo Research). RNA was converted into cDNA (Thermo RevertAid Reverse Transcriptase) and used

254 as template for qPCR (Qiagen RT2 SYBR green qPCR Mastermix). Primers are listed in Supplemental
255 Table S1. Data was collected on a 7500 Fast Dx Real-Time PCR Instrument (Applied Biosystems).

256 **Plasmids**

257 Full length, domain deletion, and functional mutation human CNP gene versions were cloned into
258 a pCAGGS-HA as described previously [44]. Briefly, genes were cloned into pCAGGS-HA vectors on
259 EcoR1/Xma1 sites, resulting in a C-terminal HA epitope tag. Genes or gene fragments were PCR
260 amplified with primers (Supplemental Table S2) to allow for In-Fusion gene cloning (Takara Bio)
261 according to the manufacturer's instructions. For functional mutant clones, primer directed mutagenesis
262 was performed and gene fragments were combined during the In-fusion cloning process.

263 **SARS-CoV-2 inhibition by CNP deletion/mutation constructs**

264 All CNP-mediated SARS-CoV-2 inhibition analysis was performed using HEK293T/hACE2
265 cells. HEK293T/hACE2 cells were seeded in 24-well plates pre-coated with 50µg/mL Rat Tail Collagen I
266 (Gibco), according to the manufacturer's instructions. At the time of seeding, pCAGGS-HA plasmids
267 were transfected using 1µL TransIT 2020 (Mirus) per 100µg plasmid and incubated overnight. Cells were
268 then infected with SARS-CoV-2/WA1 (MOI = 0.01). Supernatants were collected 48-hours post-infection
269 and SARS-CoV-2 titers determined by VeroT plaque assay.

270 **Stable Cell Line Generation**

271 Lentiviruses expressing HA-tagged CNP or HA-tagged GFP were obtained from VectorBuilder,
272 Inc. HEK293T/hACE2 cells were transduced with lentiviruses (MOI = 3) pre-treated with 10µg/mL
273 Polybrene (VectorBuilder, Inc.). Transduced cells were selected by resistance to 10µg/mL Blasticidin
274 (InvivoGen) for 10 days, followed by continued maintenance in cell culture media supplemented with
275 10µg/mL Blasticidin (InvivoGen).

276 **SARS-CoV-2 Lifecycle Inhibition Analysis**

277 HEK293T/hACE2 cells stably expressing CNP/HA or GFP/HA were seeded in 24-well plates
278 pre-coated with 50µg/mL Rat Tail Collagen I (Gibco), according to the manufacturer's instructions, or in
279 Tab-Tek II CC2 chamber slides (Thermo Fisher Scientific). Separate wells were seeded for each assay to

280 process. The following day, cells were infected with SARS-CoV-2/WA1 (MOI = 5) for a 45-minute
281 absorption period, followed by inoculum removal and washing with fresh cell culture media. Cells were
282 then maintained at cell culture conditions until collection.

283 At 6-hours post infection, cells were washed with complete cell culture media and then lysed in
284 TRIzol (Ambion). Lysates were stored at -80°C until processing for RT-qPCR.

285 At 12-hours post-infection, cells were washed with complete cell culture media and then lysed in
286 complete lysis buffer containing 20mM Tris-HCl, 150mM NaCl, 1% Nonidet P-40 (v/v), 0.5% Sodium
287 Dodecyl Sulphate (w/v), 5mM EDTA, and 1 X complete protease inhibitor (Roche), for 5 minutes at
288 room temperature. Lysates were collected and then boiled twice at 95°C for 30 minutes. Lysates were
289 then centrifuged at 21,000 x g for 20 minutes followed by supernatant collection. Supernatants were and
290 stored at -80°C until ready to process by Western Blot (below).

291 At 12-hours post-infection, cells were fixed in 2% paraformaldehyde for 1 hour at 4°C and then
292 washes once with 1 x PBS. Fixed cells were stored at 4°C until processing for immunofluorescent
293 microscopy and confocal microscopy.

294 At 18-hours post-infection, supernatants were collected for extracellular SARS-CoV-2 titer
295 determination and stored at -80°C until VeroT plaque assay processing. Cells were then washed once with
296 complete cell culture media followed by addition of 120µL of complete cell culture media. Cells were
297 then freeze-thawed three times to burst cells and lysates were collected for intracellular SARS-CoV-2 titer
298 determination and stored at -80°C until VeroT plaque assay processing.

299 **Western Blot**

300 Western blots were performed similar to what has been described previously [45]. Cell lysates
301 were run on Mini-PROTEAN TGX Precast Gels (BioRad) and tank blotted onto PVDF membranes
302 according to the manufacturer's instructions. Following blotting, membranes were blocked in blocking
303 buffer, TBST (TBS (from where?) with 0.1% Tween 20 (v/v) (from where)) and 5% milk (w/v) (from
304 where), for 1 hour at room temperature. Membranes were then incubated in primary antibody overnight at
305 4°C followed by 3 x 10-minute washes with TBST. Membranes were then incubated with diluted

306 secondary antibodies for 1 hour at room temperature followed by 5 x 10-minute washes with TBST.
307 Membranes were then developed with ECL (Cytiva) and imaged with a CCD camera. All antibodies
308 (Supplemental Table S3) were diluted in blocking buffer.

309 **Immunofluorescence Microscopy and Confocal Microscopy**

310 Paraformaldehyde fixed cells were permeabilized in PBS with 0.3% Triton-100 for 30 minutes at
311 room temperature. Cells were then blocked in blocking buffer, PBS containing 5% BSA (w/v), for 1 hour
312 at room temperature. Cells were then incubated with diluted primary antibody overnight at 4°C followed
313 by 3 x 10-minute washes with wash buffer, PBS containing 1% BSA (w/v) and 0.1% Tween-20 (v/v).
314 Cells were then incubated with diluted secondary antibodies for 1 hour at room temperature followed by 3
315 x 10-minute washes with wash buffer and 2 x 10-minute washes in PBS. Coverslips were then mounted
316 with ProLong Glass Antifade Mountant with NucBlue (Invitrogen) for at least 30 minutes at room
317 temperature. All antibodies (Supplemental Table S3) were diluted in blocking buffer.

318 Stained slides were visualized using a Revolve fluorescent microscope (Echo) or a W-1 Spinning
319 Disk confocal microscope (Nikon). Images collected by confocal microscopy were 2-D deconvoluted
320 using the W-1 spinning disk software and analyzed using ImageJ (NIH).

321 **Mitochondrial Function Assay Design**

322 HEK293T/hACE2 cells were seeded in Tab-Tek II CC2 chamber slides (Thermo Fisher
323 Scientific). At the time of seeding, pCAGGS-HA plasmids were transfected using 1µL TransIT 2020
324 (Mirus) per 100µg plasmid and maintained at cell culture conditions overnight. Cells were then infected
325 with SARS-CoV-2/WA1 (MOI = 0.1). Mitochondrial function assays (described below) were then
326 processed at 6-hours post-infection.

327 **JC-10 Staining**

328 At 6-hours post-infection, JC-10 staining was completed using the mitochondria membrane
329 potential kit (Sigma-Aldrich) according to the manufacturer's instructions. Slides were then washed once
330 with 1 x HBBS and fixed in 2% paraformaldehyde for 30 minutes at room temperature. Coverslips were

331 then mounted with ProLong Glass Antifade Mountant with NucBlue (Invitrogen) for 30 minutes at room
332 temperature and visualized immediately using a Revolve fluorescent microscope (Echo).

333 **TMRM Staining**

334 At 6-hours post-infection, opening of the mitochondrial permeabilization transition pore (mPTP)
335 was visualized by tetramethylrhodamine methyl ester perchlorate (TMRM) staining (Sigma). Cells were
336 washed once with 1 x HBBS (Gibco) followed by incubation with 100 nM TMRM diluted in 1 x HBBS
337 for 30 minutes at 37°C. Slides were then washed once with 1 x PBS and fixed in 2% paraformaldehyde
338 for 30 minutes at room temperature. Coverslips were then mounted with ProLong Glass Antifade
339 Mountant with NucBlue (Invitrogen) for 30 minutes at room temperature and visualized immediately
340 using a Revolve fluorescent microscope (Echo).

341 **Reactive Oxygen Species Staining (H2DCFDA)**

342 At 6-hours post-infection, intracellular reactive oxygen species levels were visualized by
343 H_2DCFDA staining (Invitrogen) according to the manufacturer's instructions. Briefly, cells were washed
344 twice with 1 x HBBS (Gibco) followed by incubation with 2.5μM H_2DCFDA diluted in 1 x HBBS for 30
345 minutes at 37°C. Slides were then washed three times with 1 x PBS and fixed in 2% paraformaldehyde
346 for 30 minutes at room temperature. Coverslips were then mounted with ProLong Glass Antifade
347 Mountant with NucBlue (Invitrogen) for 30 minutes at room temperature and visualized immediately
348 using a Revolve fluorescent microscope (Echo).

349 **Reactive oxygen species Addition and Cyclospoirin-A Treatment Experiments**

350 HEK293T/hACE2 cells stably expressing either CNP/HA or GFP/HA were seeded and infected
351 with SARS-CoV-2/WA1 as described in "SARS-CoV-2 Lifecycle Inhibition Analysis". At 3-hours post-
352 infection, a concentration range of hydrogen peroxide (Sigma Aldrich) or vehicle (water) was added to
353 infected cells. At 18-hours post infection, supernatants and cell lysates were collected for
354 extracellular/intracellular SARS-CoV-2 titer determination as described in "SARS-CoV-2 Lifecycle
355 Inhibition Analysis" and stored at -80°C until further processing.

356 For Cyclosporin A treatment studies, HEK293T/hACE2 cells stably expressing either CNP/HA or
357 GFP/HA were seeded and infected with SARS-CoV-2/WA1 as described in "SARS-CoV-2 Lifecycle
358 Inhibition Analysis". After washing away unbound virus, fresh media containing 10µM Cyclosporin A
359 (SelleckChem) or 0.01% DMSO as a vehicle control was added to cells. At 18-hours post infection, cell
360 lysates were collected for intracellular SARS-CoV-2 titer determination as described in "SARS-CoV-2
361 Lifecycle Inhibition Analysis" and stored at -80°C until further processing.

362 **CNP overexpression antiviral Testing *in vivo***

363 Two mammalian gene expression recombinant Adenovirus serotype 5 (rAd5) viral vectors were
364 prepared by and obtained from VectorBuilder Inc. to dually express hACE2 and either: (1) HA-tagged
365 hCNP (Ad/CNP); or (2) HA-tagged enhanced green fluorescent protein (Ad/eGFP). To confirm rAd5
366 transduction, 8-10 week old BALB/c laboratory mice were anaesthetized with a mix of xylazine and
367 ketamine diluted in phosphate buffered saline prior to intranasal transduction with 1 x 10^8 PFU of either
368 Ad/CNP or Ad/eGFP and weights were recorded (Fig. 5a). At 3-days post-rAd5-transduction, weights
369 were again recorded and lungs harvested and sectioned for the following: (1) fixed in 4%
370 paraformaldehyde for histopathological analysis and immunofluorescent staining; and (2) homogenized in
371 TRIzol for RT-qPCR analysis. Homogenization occurred using 1.0 mm glass beads (Sigma Aldrich) and
372 a Beadruptor (Omni International Inc.).

373 For SARS-CoV-2 antiviral testing, 8-10 week old BALB/c laboratory mice were anaesthetized
374 with a mix of xylazine and ketamine diluted in phosphate buffered saline prior to intranasal transduction
375 with 1 x 10^8 PFU of either Ad/CNP or Ad/eGFP. Three days later, mice were again anaesthetized with a
376 mix of xylazine and ketamine diluted in phosphate buffered saline prior to intranasal inoculation with
377 either 1 x 10^3 PFU or 1 x 10^5 PFU of SARS-CoV-2/WA1 (Fig. 6a). Control mice were also mock infected
378 with 1 x PBS. Weights were collected daily following SARS-CoV-2 infection and 5 mice sacrificed on 2
379 dpi and 4 dpi for each treatment group. Lungs were harvested and sectioned for the following: (1) fixed in
380 4% paraformaldehyde for histopathological analysis; (2) homogenized in TRIzol for RT-qPCR analysis;

381 and (3) homogenized in PBS for plaque assay processing. Homogenization occurred using 1.0 mm glass
382 beads (Sigma Aldrich) and a Beadruptor (Omni International Inc.).

383 **Histopathology**

384 Histopathology was processed as described previously [46]. Lung sections were fixed in 4%
385 paraformaldehyde in phosphate-buffered saline for a minimum of 48 h, after which they were sent to the
386 Histology Core at the University of Maryland, Baltimore, for paraffin embedding and sectioning. Five-
387 micrometer sections were prepared and used for hematoxylin and eosin (H&E) staining by the Histology
388 Core Services. Sections were imaged at 10x magnification and assembled into figures using Adobe
389 Photoshop and Illustrator software.

390 **Immunofluorescent staining of mouse lung histology slides**

391 Lung sections were fixed in 4% paraformaldehyde in phosphate-buffered saline for a minimum of
392 48 h, after which they were sent to the Histology Core at the University of Maryland, Baltimore, for
393 paraffin embedding and sectioning. Slides were then deparaffinized with 2 x 5-minute washes in Xylenes
394 (Sigma Aldrich) followed by rehydration with decreasing concentrations of ethanol in water. Following
395 rehydration, antigen retrieval was completed by boiling samples in citrate buffer (Millipore Sigma) for 5
396 minutes followed with removal of heat and an additional 15-minute incubation. Samples were then
397 washed twice with ddH2O.

398 Slides were then stained for immunofluorescent imaging. All incubations were performed in a humidified
399 chamber. Slides were blocked in blocking buffer, PBS++ (1 x PBS with 1mM MgCl and 1mM $CaCl_2$)
400 with 1% (w/v) BSA, for 1 hour at room temperature. Following blocking, slides were incubated overnight
401 at 4°C with diluted primary antibody followed by 3 x 10-minute washes with PBS++. Slides were then
402 incubated for 1 hour at room temperature with diluted secondary antibodies, followed by 3 x 10-minute
403 washes with PBS++. Coverslips were then mounted with ProLong Glass Antifade Mountant with
404 NucBlue (Invitrogen) for at least 30 minutes at room temperature and visualized using a Revolve
405 fluorescent microscope (Echo). All antibodies (Supplemental Table S3) were diluted in blocking buffer.
406

Acknowledgements

The authors would like to thank the Histology Core at the University of Maryland, Baltimore for histology processing.

Funding

This work is partially funded by NIH R01 AI148166

Contributions

J.L. and M.B.F. contributed to conceptualization of experiments. J.L., V.M.M., J.A., and M.B.F. contributed to the generation of data and analysis and interpretation of the results. J.L., V.M.M, and J.A. performed the experiments. M.B.F. coordinated the projects. J.L. and M.B.F. contributed to drafting and making critical revisions with the help of all authors listed on this manuscript.

Competing Interests Statement

M.B.F. is on the scientific advisory board of Aikido Pharma and has collaborative research agreements with Novavax, AstraZeneca, Regeneron, and Irazu Bio. These do not have any effect on the planning or interpretations of the work presented in this manuscript.

References

1. Huang, C., et al., *Clinical features of patients infected with 2019 novel coronavirus in Wuhan, China.* Lancet, 2020. **395**(10223): p. 497-506.
2. Zhou, P., et al., *A pneumonia outbreak associated with a new coronavirus of probable bat origin.* Nature, 2020. **579**(7798): p. 270-273.

430 3. Zhu, N., et al., *A Novel Coronavirus from Patients with Pneumonia in China, 2019.* N Engl J
431 Med, 2020. **382**(8): p. 727-733.
432 4. Dong, E., H. Du, and L. Gardner, *An interactive web-based dashboard to track COVID-19 in real*
433 *time.* Lancet Infect Dis, 2020. **20**(5): p. 533-534.
434 5. Dong, E., H. Du, and L. Gardner. *COVID-19 Dashboard*. 2020 [cited 2023 March 02]; Available
435 from: https://coronavirus.jhu.edu/map.html.
436 6. Dittmar, M., et al., *Drug repurposing screens reveal cell-type-specific entry pathways and FDA-*
437 *approved drugs active against SARS-Cov-2.* Cell Rep, 2021. **35**(1): p. 108959.
438 7. Riva, L., et al., *Discovery of SARS-CoV-2 antiviral drugs through large-scale compound*
439 *repurposing.* Nature, 2020. **586**(7827): p. 113-119.
440 8. Weston, S., et al., *Broad Anti-coronavirus Activity of Food and Drug Administration-Approved*
441 *Drugs against SARS-CoV-2 In Vitro and SARS-CoV In Vivo.* J Virol, 2020. **94**(21).
442 9. FDA. *FDA Approves First Treatment for COVID-19*. 2020 [cited 2023 MARCH 7]; Available
443 from: https://www.fda.gov/news-events/press-announcements/fda-approves-first-treatment-covid-
444 19.
445 10. FDA. *Lagevrio (molnupiravir) Letter of Authorization*. 2022; Available from:
446 https://www.fda.gov/media/155053/download.
447 11. FDA. *Paxlovid (nirmatrelvir tablets and ritonavir tablets, co-packaged for oral use) Letter of*
448 *Authorization*. 2022 [cited 2023 MARCH 7]; Available from:
449 https://www.fda.gov/media/155049/download.
450 12. FDA. *Bamlanivimab and Etesevimab Letter of Authhorization*. 2022 [cited 2023 MARCH 7];
451 Available from: https://www.fda.gov/media/145801/download.
452 13. FDA. *Evusheld (tixagevimab co-packaged with cilgavimab) Letter of Authorization*. 2022 [cited
453 2023 MARCH 7]; Available from: https://www.fda.gov/media/154704/download.
454 14. FDA. *Sotrovimab Letter of Authorization*. 2022 [cited 2023 MARCH 7]; Available from:
455 https://www.fda.gov/media/149532/download.

456 15. Belouzard, S., V.C. Chu, and G.R. Whittaker, *Activation of the SARS coronavirus spike protein*
457 *via sequential proteolytic cleavage at two distinct sites.* Proc Natl Acad Sci U S A, 2009.
458 **106**(14): p. 5871-6.
459 16. Gierer, S., et al., *The spike protein of the emerging betacoronavirus EMC uses a novel*
460 *coronavirus receptor for entry, can be activated by TMPRSS2, and is targeted by neutralizing*
461 *antibodies.* J Virol, 2013. **87**(10): p. 5502-11.
462 17. Hoffmann, M., et al., *SARS-CoV-2 Cell Entry Depends on ACE2 and TMPRSS2 and Is Blocked*
463 *by a Clinically Proven Protease Inhibitor.* Cell, 2020. **181**(2): p. 271-280.e8.
464 18. Letko, M., A. Marzi, and V. Munster, *Functional assessment of cell entry and receptor usage for*
465 *SARS-CoV-2 and other lineage B betacoronaviruses.* Nat Microbiol, 2020. **5**(4): p. 562-569.
466 19. Matsuyama, S., et al., *Efficient activation of the severe acute respiratory syndrome coronavirus*
467 *spike protein by the transmembrane protease TMPRSS2.* J Virol, 2010. **84**(24): p. 12658-64.
468 20. Ou, X., et al., *Characterization of spike glycoprotein of SARS-CoV-2 on virus entry and its*
469 *immune cross-reactivity with SARS-CoV.* Nat Commun, 2020. **11**(1): p. 1620.
470 21. Walls, A.C., et al., *Structure, Function, and Antigenicity of the SARS-CoV-2 Spike Glycoprotein.*
471 Cell, 2020. **181**(2): p. 281-292.e6.
472 22. Chan, J.F., et al., *Genomic characterization of the 2019 novel human-pathogenic coronavirus*
473 *isolated from a patient with atypical pneumonia after visiting Wuhan.* Emerg Microbes Infect,
474 2020. **9**(1): p. 221-236.
475 23. Finkel, Y., et al., *The coding capacity of SARS-CoV-2.* Nature, 2021. **589**(7840): p. 125-130.
476 24. Snijder, E.J., et al., *A unifying structural and functional model of the coronavirus replication*
477 *organelle: Tracking down RNA synthesis.* PLoS Biol, 2020. **18**(6): p. e3000715.
478 25. Wolff, G., et al., *A molecular pore spans the double membrane of the coronavirus replication*
479 *organelle.* Science, 2020. **369**(6509): p. 1395-1398.

480 26. Viehweger, A., et al., *Direct RNA nanopore sequencing of full-length coronavirus genomes*
481 *provides novel insights into structural variants and enables modification analysis.* Genome Res,
482 2019. **29**(9): p. 1545-1554.
483 27. de Haan, C.A. and P.J. Rottier, *Molecular interactions in the assembly of coronaviruses.* Adv
484 Virus Res, 2005. **64**: p. 165-230.
485 28. Klein, S., et al., *SARS-CoV-2 structure and replication characterized by in situ cryo-electron*
486 *tomography.* Nat Commun, 2020. **11**(1): p. 5885.
487 29. Stertz, S., et al., *The intracellular sites of early replication and budding of SARS-coronavirus.*
488 Virology, 2007. **361**(2): p. 304-15.
489 30. Martin-Sancho, L., et al., *Functional landscape of SARS-CoV-2 cellular restriction.* Mol Cell,
490 2021. **81**(12): p. 2656-2668.e8.
491 31. de Monasterio-Schrader, P., et al., *Systematic approaches to central nervous system myelin.* Cell
492 Mol Life Sci, 2012. **69**(17): p. 2879-94.
493 32. Rösener, M., et al., *2',3'-cyclic nucleotide 3'-phosphodiesterase: a novel candidate autoantigen in*
494 *demyelinating diseases.* J Neuroimmunol, 1997. **75**(1-2): p. 28-34.
495 33. Uhlén, M., et al., *Proteomics. Tissue-based map of the human proteome.* Science, 2015.
496 **347**(6220): p. 1260419.
497 34. Drummond, G.I. and S. Perrott-Yee, *Enzymatic hydrolysis of adenosine 3',5'-phosphoric acid.* J
498 Biol Chem, 1961. **236**: p. 1126-9.
499 35. Azarashvili, T., et al., *Ca2+-dependent permeability transition regulation in rat brain*
500 *mitochondria by 2',3'-cyclic nucleotides and 2',3'-cyclic nucleotide 3'-phosphodiesterase.* Am J
501 Physiol Cell Physiol, 2009. **296**(6): p. C1428-39.
502 36. Baburina, Y., et al., *Mitochondrial 2', 3'-cyclic nucleotide 3'-phosphodiesterase (CNP) interacts*
503 *with mPTP modulators and functional complexes (I-V) coupled with release of apoptotic factors.*
504 Neurochem Int, 2015. **90**: p. 46-55.

505 37. Baburina, Y., et al., *2',3'-Cyclic nucleotide 3'-phosphodiesterase as a messenger of protection of*
506 *the mitochondrial function during melatonin treatment in aging.* Biochim Biophys Acta
507 Biomembr, 2017. **1859**(1): p. 94-103.
508 38. McFerran, B. and R. Burgoyne, *2',3'-Cyclic nucleotide 3'-phosphodiesterase is associated with*
509 *mitochondria in diverse adrenal cell types.* J Cell Sci, 1997. **110 (Pt 23)**: p. 2979-85.
510 39. Shang, C., et al., *SARS-CoV-2 Causes Mitochondrial Dysfunction and Mitophagy Impairment.*
511 Front Microbiol, 2021. **12**: p. 780768.
512 40. Lu, S., et al., *The SARS-CoV-2 nucleocapsid phosphoprotein forms mutually exclusive*
513 *condensates with RNA and the membrane-associated M protein.* Nat Commun, 2021. **12**(1): p.
514 502.
515 41. Kell, D.B. and E. Pretorius, *The potential role of ischaemia-reperfusion injury in chronic,*
516 *relapsing diseases such as rheumatoid arthritis, Long COVID, and ME/CFS: evidence,*
517 *mechanisms, and therapeutic implications.* Biochem J, 2022. **479**(16): p. 1653-1708.
518 42. Matsuyama, S., et al., *Enhanced isolation of SARS-CoV-2 by TMPRSS2-expressing cells.* Proc
519 Natl Acad Sci U S A, 2020. **117**(13): p. 7001-7003.
520 43. Coleman, C.M. and M.B. Frieman, *Growth and Quantification of MERS-CoV Infection.* Curr
521 Protoc Microbiol, 2015. **37**(1): p. 15e.2.1-9.
522 44. Weston, S., et al., *The SKI complex is a broad-spectrum, host-directed antiviral drug target for*
523 *coronaviruses, influenza, and filoviruses.* Proc Natl Acad Sci U S A, 2020. **117**(48): p. 30687-
524 30698.
525 45. Weston, S., et al., *A Yeast Suppressor Screen Used To Identify Mammalian SIRT1 as a Proviral*
526 *Factor for Middle East Respiratory Syndrome Coronavirus Replication.* J Virol, 2019. **93**(16).
527 46. Schultz, D.C., et al., *Pyrimidine inhibitors synergize with nucleoside analogues to block SARS-*
528 *CoV-2.* Nature, 2022. **604**(7904): p. 134-140.
529

530 # Figure Legends

531 **Figure 1: CNP Overexpression inhibits generation of new SARS-CoV-2 virions.**

532 HEK293T/hACE2 cells stably overexpressing either CNP or GFP were infected with SARS-CoV-2/WA1
533 for 45-minutes followed by washing of any unbound virus. At 6-hours post-infection, intracellular SARS-
534 CoV-2 RNA levels were determined by RT-qPCR for (**a**) genomic RNA and (**b**) subgenomic RNA. (**c**) At
535 12-hours post-infection, lysates were collected and western blot staining performed for SARS-CoV-2 S,
536 SARS-CoV-2 N, and actin as a loading control. At 18-hours post-infection, plaque assays were performed
537 to determine (**d**) intracellular SARS-CoV-2 titers and (**e**) extracellular SARS-CoV-2 titers. **$p \leq 0.01$,
538 ***$p \leq 0.001$, "ns": $p > 0.5$.

539

540 **Figure 2: CNP overexpression alters SARS-CoV-2 structural protein localization during virion**
541 **assembly.**

542 HEK293T/hACE2 cells stably overexpressing either CNP or GFP were infected with SARS-CoV-2/WA1
543 for 45-minutes followed by washing of any unbound virus. At 12-hours post infection, cells were fixed,
544 immunofluorescent stained, and confocal images collected for (**a**) ERGIC53 (blue) and SARS-CoV-2 S
545 (red) or (**b**) ERGIC53 (blue) and SARS-CoV-2 N (red). ERGIC53 colocalization with SARS-CoV-2
546 structural proteins was assessed in ImageJ for (**c**) SARS-CoV-2 S or (**d**) SARS-CoV-2 N. *$p \leq 0.1$, **$p \leq$
547 0.01.

548

549 **Figure 3: CNP overexpression inhibits SARS-CoV-2-induced mitochondrial depolarization.**

550 HEK293T/hACE2 cells were infected with SARS-CoV-2/WA1 24-hours following transfection with
551 indicated plasmids. (**a**) 48-hours post-infection, supernatants were collected, and SARS-CoV-2 titers were
552 determined by plaque assay. (**b**-**c**) At 6-hours post-infection, mitochondrial function was assessed for (**b**)
553 mitochondrial depolarization with JC10 staining or (**c**) opening of the mPTP with TMRM staining. (**d**)
554 HEK293T/hACE2 cells stably overexpressing either CNP or GFP were infected with SARS-CoV-2/WA1

555 (MOI = 5) for 45-minutes followed by washing of any unbound virus. Fresh media containing 10μM
556 Cyclosporin A or DMSO was then immediately added and intracellular SARS-CoV-2 titer determined at
557 18hpi. **$p \leq 0.01$.
558
559 **Figure 4: Reactive oxygen species are important for SARS-CoV-2 virion assembly.**
560 (**a**) HEK293T/hACE2 cells were infected with SARS-CoV-2/WA1 24-hours following transfection with
561 indicated plasmids. At 6-hours post-infection, the presence of cytosolic reactive oxygen species was
562 assessed by H_2DCFDA staining. (**b-c**) HEK293T/hACE2 cells stably overexpressing either CNP or GFP
563 were infected with SARS-CoV-2/WA1 (MOI = 5) for 45-minutes followed by washing of any unbound
564 virus. At 3-hours post-infection, cells were treated with a concentration range of hydrogen peroxide. At
565 18-hours post-infection, plaque assays were performed to determine (**b**) intracellular SARS-CoV-2 titers
566 and (**c**) extracellular SARS-CoV-2 titers. *$p \leq 0.1$, **$p \leq 0.01$, *** $p \leq 0.001$, ****$p \leq 0.0001$.
567
568 **Figure 5: Validation of dual expressing adenovirus vectors in Balb/c laboratory mice.**
569 (**a**) Groups of mice were transduced intranasally with rAd5 vectors (1 x 10^8 viral particles per mouse)
570 dually expressing hACE2 and either HA-tagged CNP or HA-tagged eGFP. Image created using
571 BioRender. (**b**) Weight changes were determined at 3 days post-transduction, plotted as the group mean
572 with error bars indicating the ±SD. **c-d** Lungs were collected at 3-days post-transduction and co-stained
573 by immunofluorescence staining for (**c**) nucleus (blue) and hACE2 (green) or (**d**) nucleus (blue) and HA-
574 tag (purple). **e-f** RT-qPCR was performed for lung homogenates collected at 3-days post-transduction for
575 (**e**) hACE2 and (**f**) CNP. *$p \leq 0.1$, **$p \leq 0.01$.
576
577 **Figure 6: CNP transduction reduces SARS-CoV-2 infection in Balb/c laboratory mice.**
578 (**a**) Groups of mice were transduced intranasally with rAd5 vectors (1 x 10^8 viral particles/ mouse) dually
579 expressing hACE2 and either HA-tagged CNP or HA-tagged eGFP 3 days prior to intranasal infection
580 with SARS-CoV-2/WA1 (1 x 10^3 or 1 x 10^5 PFU/mouse). Image created using BioRender. **b-c** Infectious

581 viral loads from lung homogenates were determined by plaque assay at 2- or 4- days post SARS-CoV-2

582 challenge for the (**b**) 1 x 10^3 PFU/mouse or (**c**) 1 x 10^5 PFU/mouse challenge groups. **d-e** Virus titers were

583 also determined by RT-qPCR for sgRNA for the (**d**) 1 x 10^3 PFU/mouse or (**e**) 1 x 10^5 PFU/mouse

584 challenge groups. *** $p \leq 0.001$, ****$p \leq 0.0001$.

585

586

587 # Supplemental Table / Figures

588 **Table S1: RT-qPCR primers.**

Gene Target	Forward (5' to 3') or Company (Cat#)	Reverse (5' to 3') or Company (Cat#)	Detection Method
sgRNA (SARS2 N)	ctcttgtagatctgttctctaaacgaac	ggtccaccaaacgtaatgcg	SYBR Green
gRNA (SARS2 RdRp)	Integrated DNA Technologies (*10006860*)	Integrated DNA Technologies (10006881)	SYBR Green
Human ACE2	------- Integrated DNA Technologies (*Hs01085333_m1*) -------		SYBR Green
Human CNP	----- Integrated DNA Technologies (*Hs.PT.58.27238178*) -----		FAM Probe
Mouse GAPDH	--------- Integrated DNA Technologies (*Mm.PT.39a.1*) ----------		SYBR Green
Human GAPDH	----- Integrated DNA Technologies (*Hs.PT.39a.22214836*) -----		SYBR Green

589 Abbreviations: "sgRNA": subgenomic RNA; "gRNA": genomic RNA; "ACE2": human angiotensin

590 converting enzyme II; "CNP": human 2',3' cyclic-nucleotide 3', phosphodiesterase; "GAPDH":

591 glyceraldehyde-3-phosphate dehydrogenase;

592

593

594 **Table S2: Infusion cloning primers.**

Gene Target (mutations)	Frag.	Forward (5' to 3')	Reverse (5' to 3')
hCNP	N/A	tcattttggcaaagaattcaccatgaacagaggcttctcc	atcataagggtacatcccgggtatgatggtgcagga
hCNP-CatMut *(H251A, T253A, H330A, T332A)*	1	tcattttggcaaagaattcaccatgaacagaggcttctcc	aacttggtagcgcaagccagcacgcctgg
	2	ttgcgctaccaagttttgtgactacg	cagccgagagcgatagcggcgcggctccc
	3	tatcgctctcggctgtgca	atcataagggtacatcccgggtatgatggtgcagga
hCNP-PrenMut (*C418A*)	N/A	tcattttggcaaagaattcaccatgaacagaggcttctcc	aagggtacatcccgggtatgatggtggcggactgca aggc
hCNPΔMTS (Δ*1-20*)	N/A	ttttggcaaagaattcatgtcatcctcaggggcca	atcataagggtacatcccgggtatgatggtgcagga
hCNPΔPloop (Δ*36-148*)	N/A	agtttcccgagcccaagacggcgtgg	tgggctcgggaaactgcagctcaggc
hCNPΔCat (Δ*185-399*)	N/A	agaaggacaaaggcaaacctgtgccc	tgcctttgtccttctccagcccaggc

595 Abbreviations: "hCNP": human 2',3' cyclic-nucleotide 3', phosphodiesterase; "CatMut": catalytic site

596 mutation; "PrenMut": prenylation site mutation; "MTS", mitochondrial targeting sequence; "Cat":

597 catalytic domain;

598

599

600

601

602 **Table S3: Antibodies for *in vitro* Western Blot and Immunofluorescent staining**

Assay	Target (Detection)	Antibodies (animal, cat#, supplier)	Staining Conc.
Western Blot	**HA-tag** (HRP)	1°: Rabbit; H6908 (Sigma) 2°: Goat α-rabbit HRP; 31460 (Invitrogen)	0.6 µg/mL 0.4 µg/mL
	SARS2 S (HRP)	1°: Rabbit; NB100-56578 (Novus) 2°: Goat α-rabbit HRP; 31460 (Invitrogen)	1.0 µg/mL 0.4 µg/mL
	SARS2 N (HRP)	1°: Rabbit; 40143-R004 (Sino Biologicals) 2°: Goat α-rabbit HRP; 31460 (Invitrogen)	1.0 µg/mL 0.4 µg/mL
	Actin (HRP)	1°: Mouse; Ab7817 (Abcam) 2°: Goat α-mouse HRP; 31430 (Invitrogen)	1.0 µg/mL 0.2 µg/mL
IFA (*in vitro*)	**HA-tag** (alexa488)	1°: Chicken; Ab9111 (Abcam) 2°: Goat α-chicken 488; A11039 (Invitrogen)	1.0 µg/mL 1.0 µg/mL
	HA-tag (alexa647)	1°: Chicken, Ab9111 (Abcam) 2°: Goat α-chicken 647; A21449 (Invitrogen)	1.0 µg/mL 1.0 µg/mL
	SARS2 S (alexa594)	1°: Rabbit; NB100-56578 (Novus) 2°: Donkey α-Rabbit 594; Ab150064 (Abcam)	1.0 µg/mL 1.0 µg/mL
	SARS2 N (alexa594)	1°: Rabbit; 40143-R004 (Sino Biologicals) 2°: Donkey α-Rabbit 594; Ab150064 (Abcam)	1.0 µg/mL 1.0 µg/mL
	ERGIC53 (alexa647)	1°: Mouse; ABS300-100 (Enzo) 2°: Goat α-mouse 647; A21235 (Invitrogen)	10.0 µg/mL 1.0 µg/mL
IFA (histology)	**hACE2** (alexa488)	1°: Goat; AF933 (R&D) 2°: Rabbit α-Goat 488; Ab11078 (Abcam)	2.0 µg/mL 2.0 µg/mL
	HA-tag (alexa647)	1°: Chicken, Ab9111 (Abcam) 2°: Goat α-chicken 647; A21449 (Invitrogen)	10.0 µg/mL 2.0 µg/mL

603 Abbreviations: "Conc.": concentration; "HRP": horse radish peroxidase; "IFA": immunofluorescence
604 assay; "SARS2": SARS-CoV-2; "N": nucleocapsid protein; "S": spike protein; "hACE2": human ACE2;
605
606
607 **Figure S1: CNP overexpression validation**
608 (**a**) HA-tag staining of HEK293T/hACE2 cells transduced with lentivirus vectors expressing either HA-
609 tagged CNP or HA-tagged eGFP and maintained under selection media. (**b**) Western blots from
610 HEK293T/hACE2 cells transfected with CNP mutation and deletion plasmid constructs stained for HA-
611 tag or Actin controls.
612
613
614

615 **Figure S2: Mitochondrial Function Staining with MOCK infection images**

616 Images correspond to Figure 3. HEK293T/hACE2 cells were infected with SARS-CoV-2/WA1 or MOCK
617 infected 24-hours following transfection with indicated plasmids. At 6-hours post-infection,
618 mitochondrial function was assessed for (**a**) opening of the mPTP with TMRM staining, (**b**) reactive
619 oxygen species staining with H_2DCFDA, or (**c**) mitochondrial depolarization with JC10 staining.

FIGURE 1

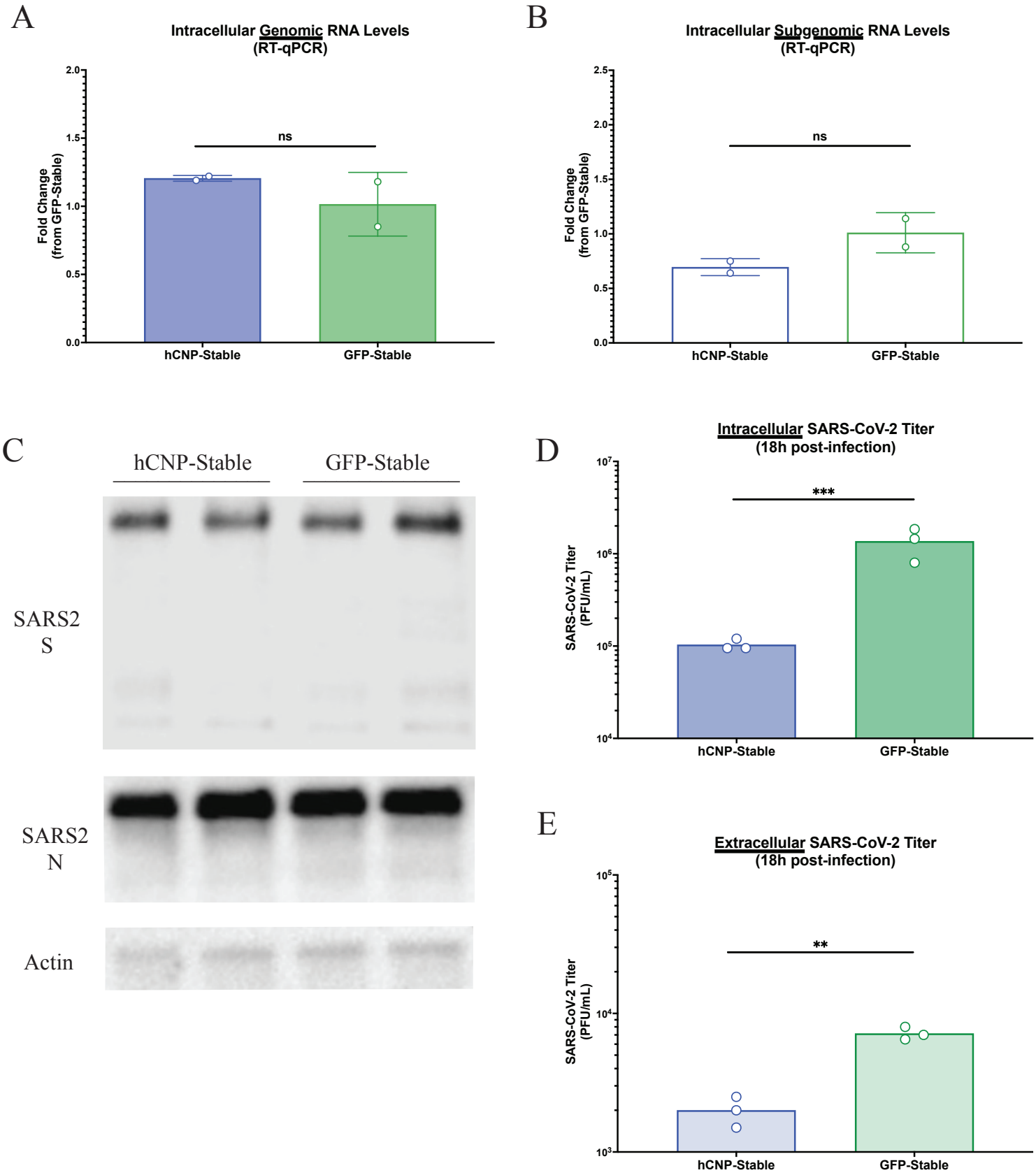
A
Intracellular Genomic RNA Levels
(RT-qPCR)
Fold Change
(from GFP-Stable)
2.0
1.5
1.0
0.5
0.0
ns
hCNP-Stable
GFP-Stable
B
Intracellular Subgenomic RNA Levels
(RT-qPCR)
Fold Change
(from GFP-Stable)
2.5
2.0
1.5
1.0
0.5
0.0
ns
hCNP-Stable
GFP-Stable
C
hCNP-Stable
GFP-Stable
SARS2
S
SARS2
N
Actin
D
Intracellular SARS-CoV-2 Titer
(18h post-infection)
SARS-CoV-2 Titer
(PFU/mL)
10^7
10^6
10^5
10^4
***
hCNP-Stable
GFP-Stable
E
Extracellular SARS-CoV-2 Titer
(18h post-infection)
SARS-CoV-2 Titer
(PFU/mL)
10^5
10^4
10^3
**
hCNP-Stable
GFP-Stable

FIGURE 2

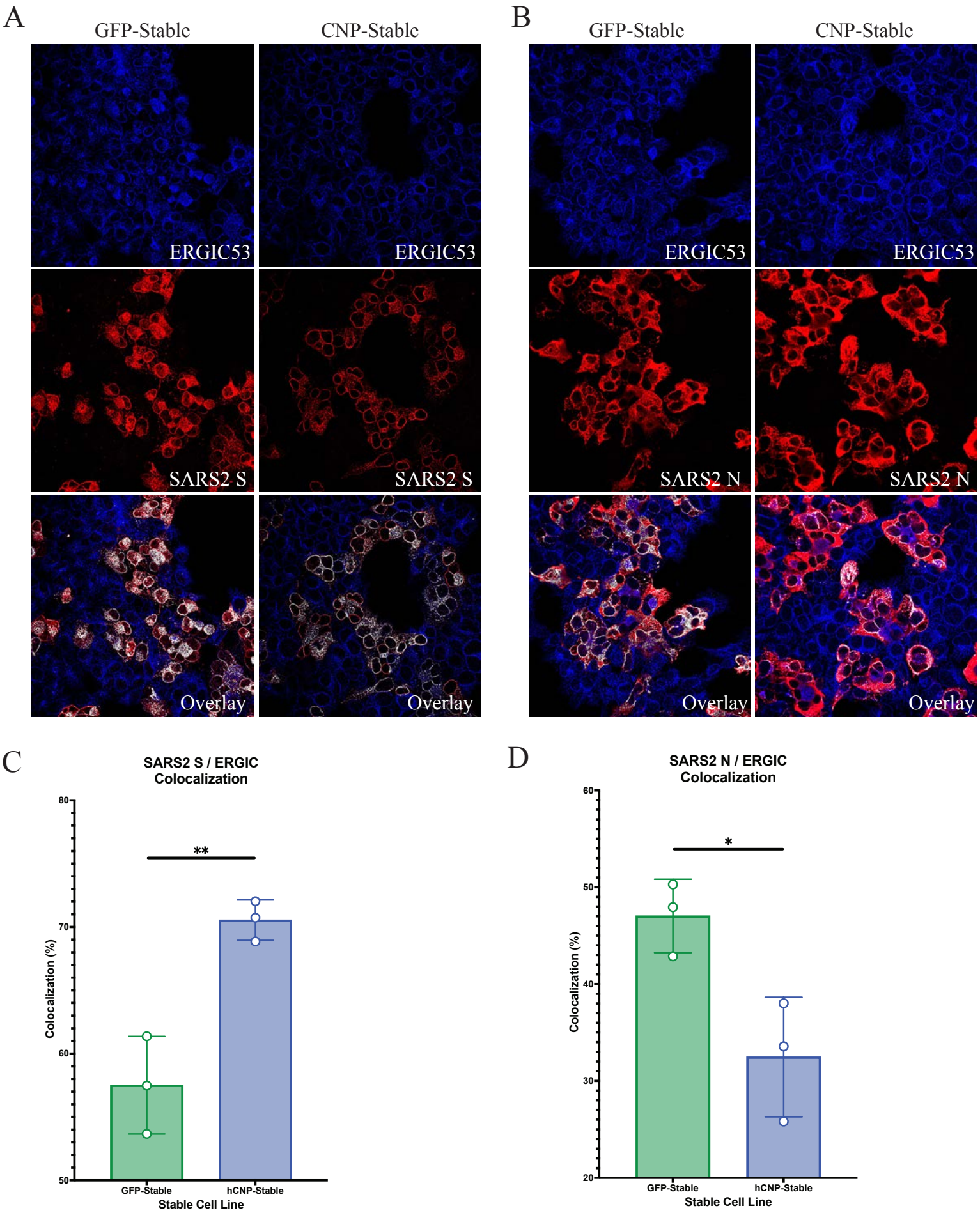
A
GFP-Stable
CNP-Stable
ERGIC53
ERGIC53
SARS2 S
SARS2 S
Overlay
Overlay
B
GFP-Stable
CNP-Stable
ERGIC53
ERGIC53
SARS2 N
SARS2 N
Overlay
Overlay
C
SARS2 S / ERGIC
Colocalization
Colocalization (%)
80
70
60
50
**
GFP-Stable
hCNP-Stable
Stable Cell Line
D
SARS2 N / ERGIC
Colocalization
Colocalization (%)
60
50
40
30
20
*
GFP-Stable
hCNP-Stable
Stable Cell Line

FIGURE 3

A

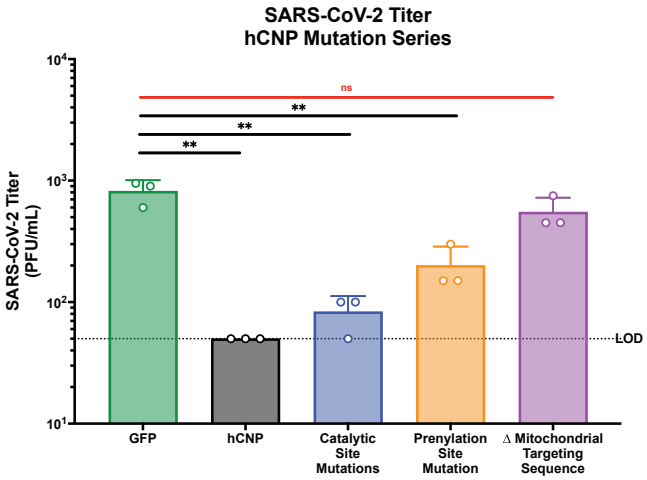

B

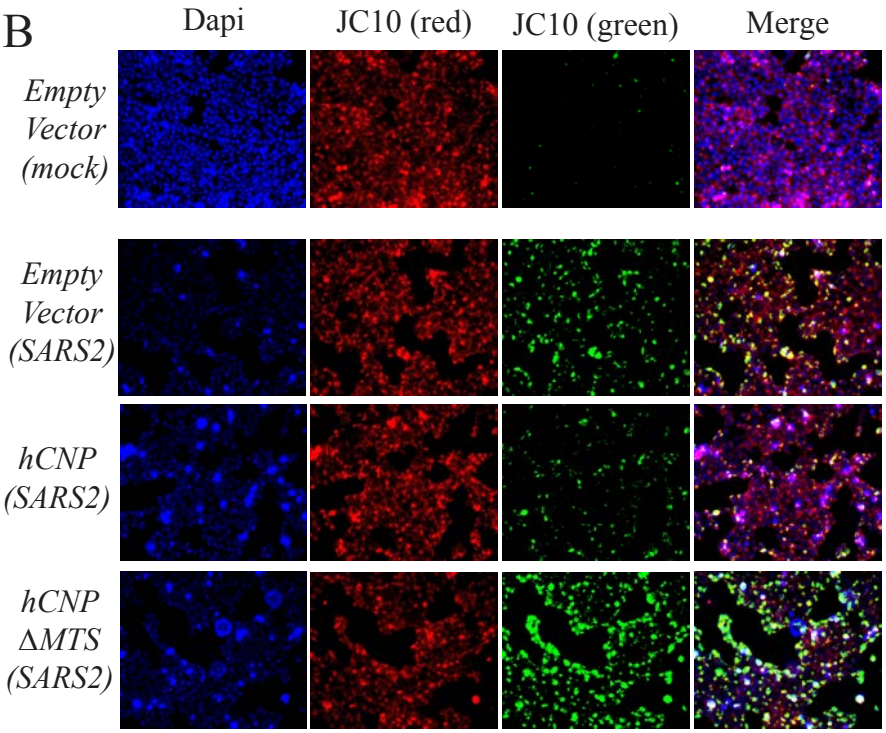

C

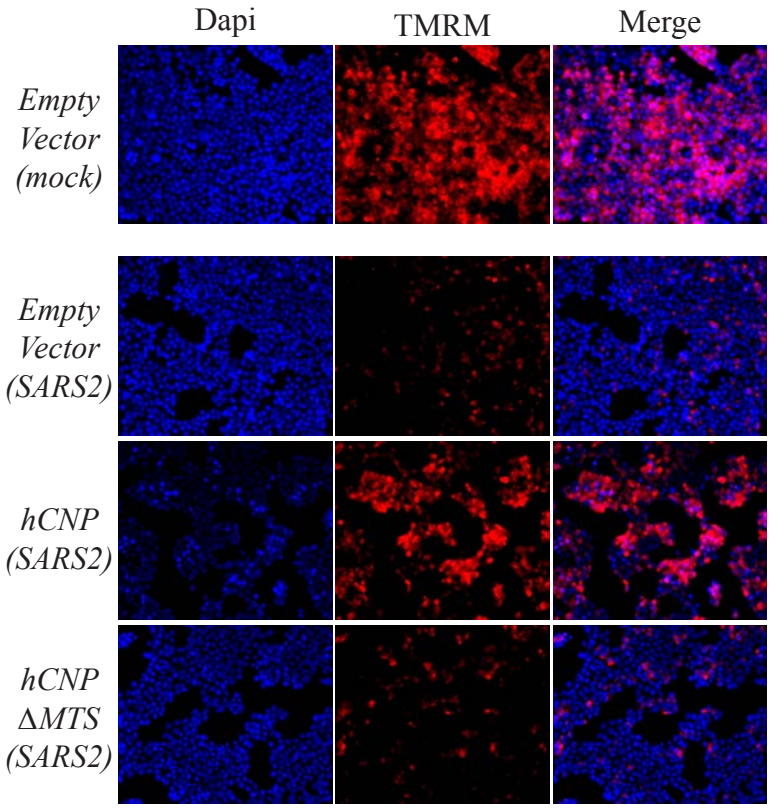

D

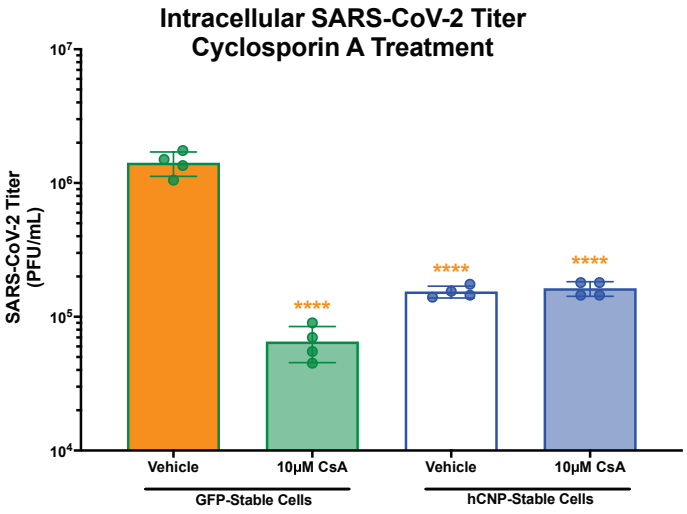

FIGURE 4

A

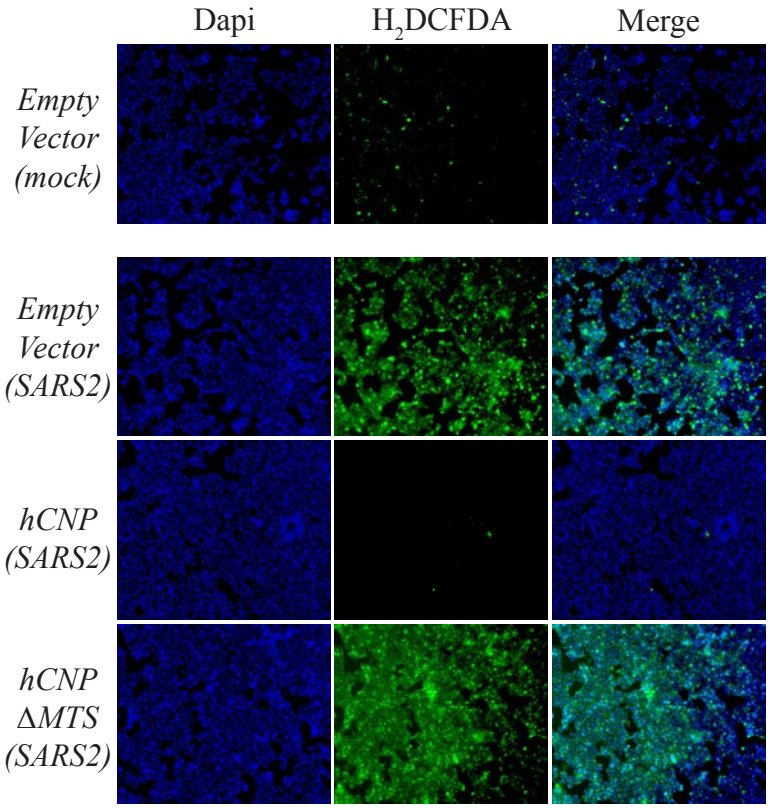
Dapi
H2DCFDA
Merge
Empty Vector (mock)
Empty Vector (SARS2)
hCNP (SARS2)
hCNP ΔMTS (SARS2)

B

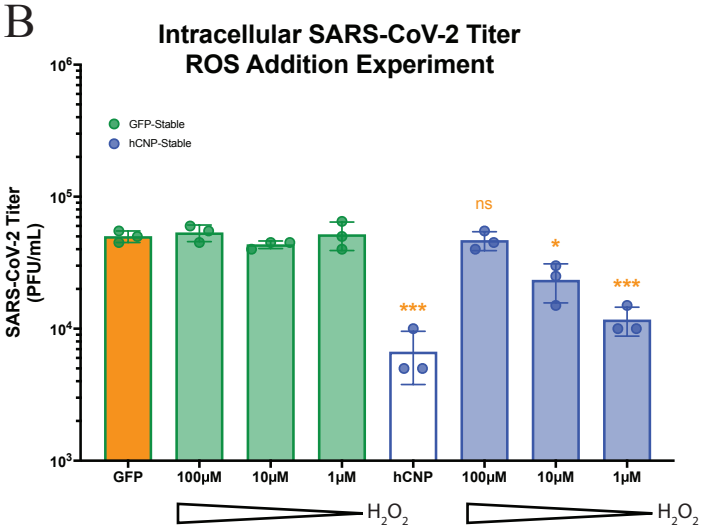
Intracellular SARS-CoV-2 Titer
ROS Addition Experiment
GFP-Stable
hCNP-Stable
SARS-CoV-2 Titer (PFU/mL)
10^6
10^5
10^4
10^3
***
ns
*
***
GFP
100μM
10μM
1μM
hCNP
100μM
10μM
1μM
H2O2
H2O2

C

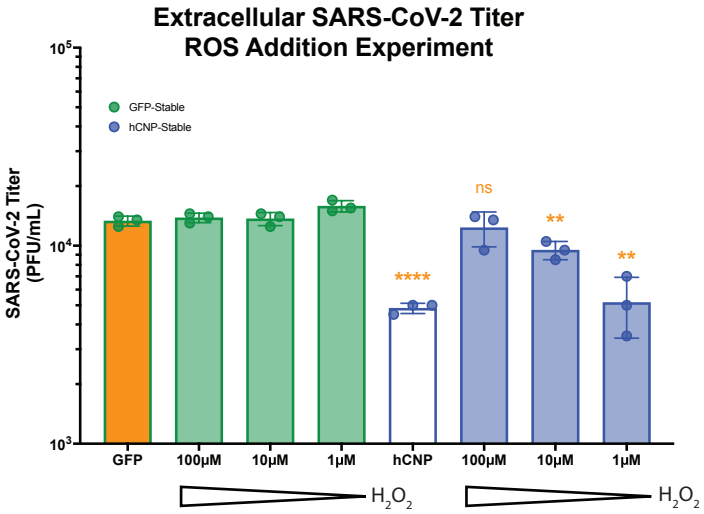
Extracellular SARS-CoV-2 Titer
ROS Addition Experiment
GFP-Stable
hCNP-Stable
SARS-CoV-2 Titer (PFU/mL)
10^5
10^4
10^3
****
ns
**
**
GFP
100μM
10μM
1μM
hCNP
100μM
10μM
1μM
H2O2
H2O2

FIGURE 5

A

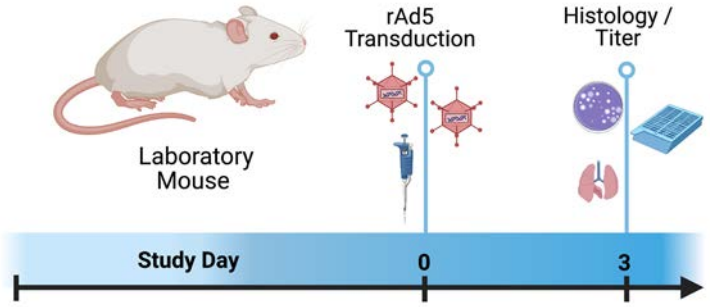

B

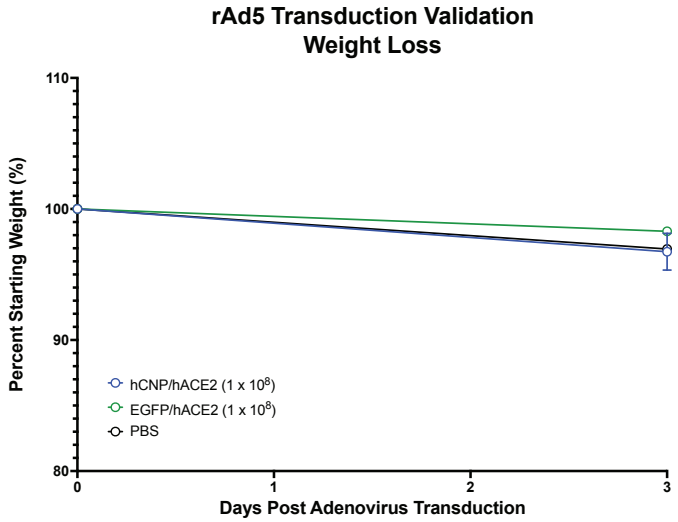

C

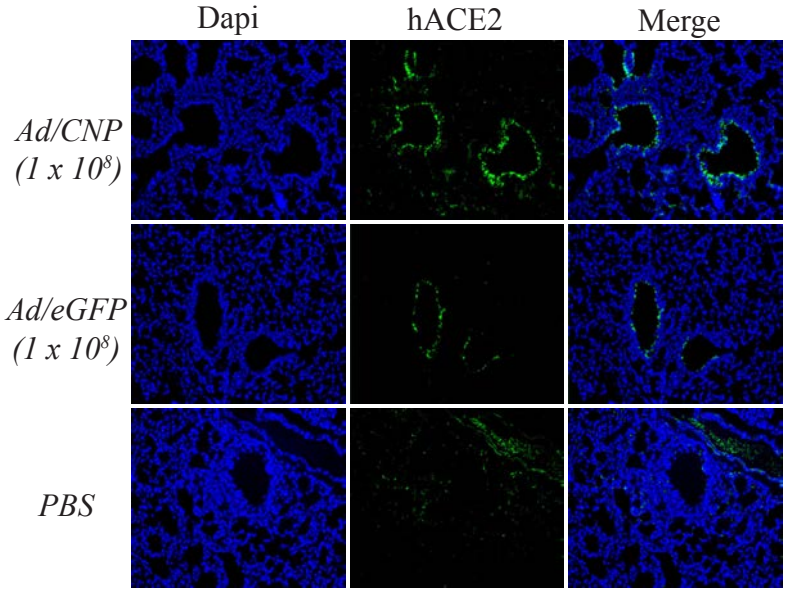

D

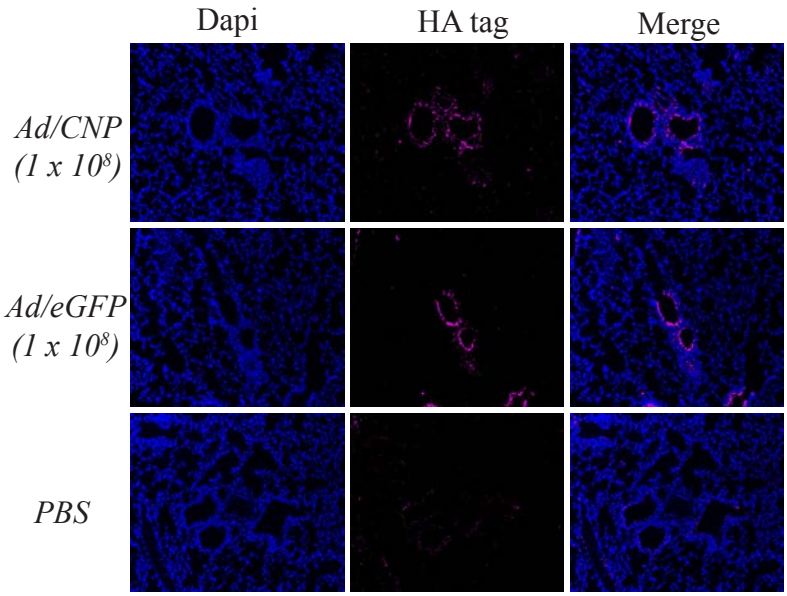

E

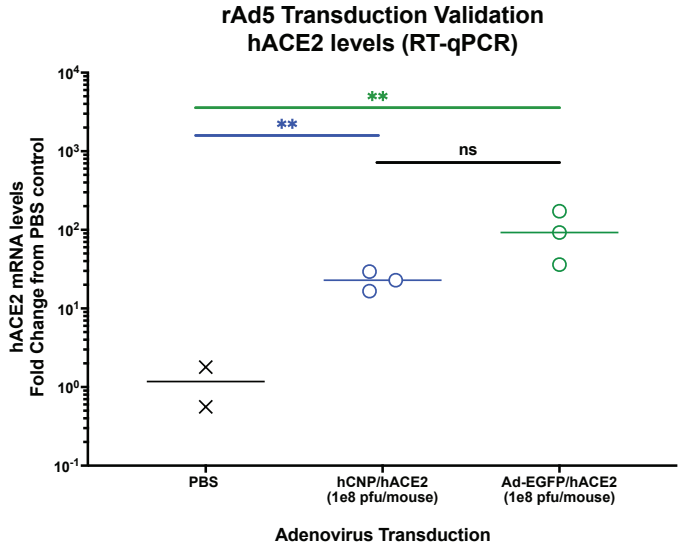

F

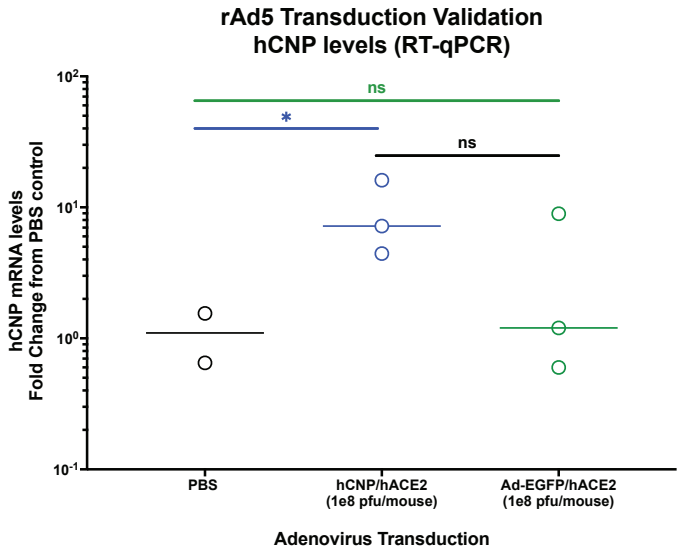

FIGURE 6

A

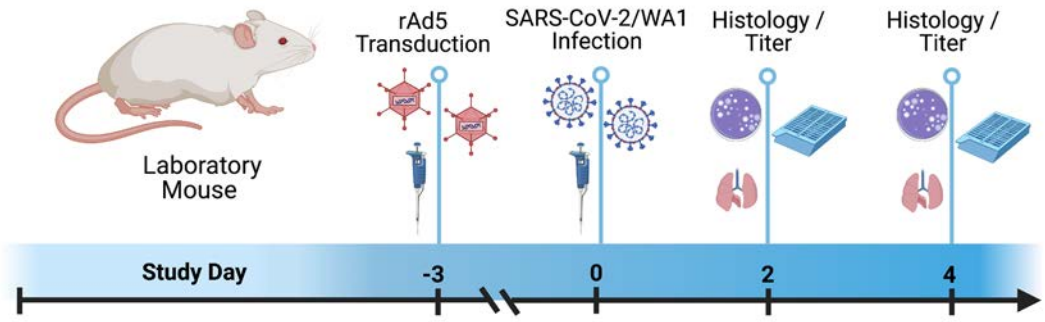

B

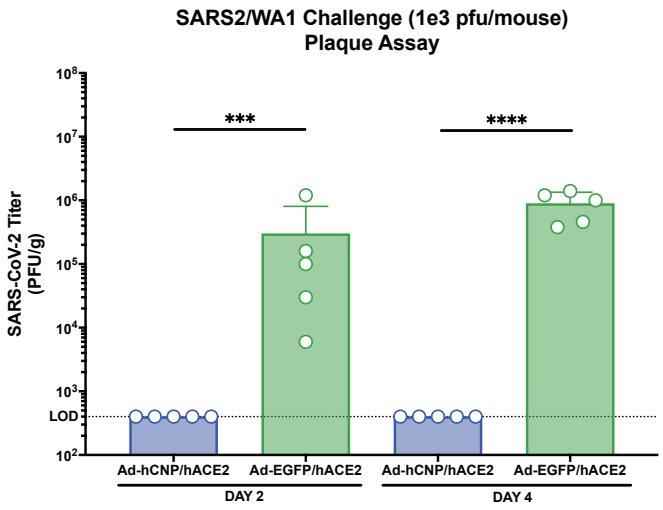

C

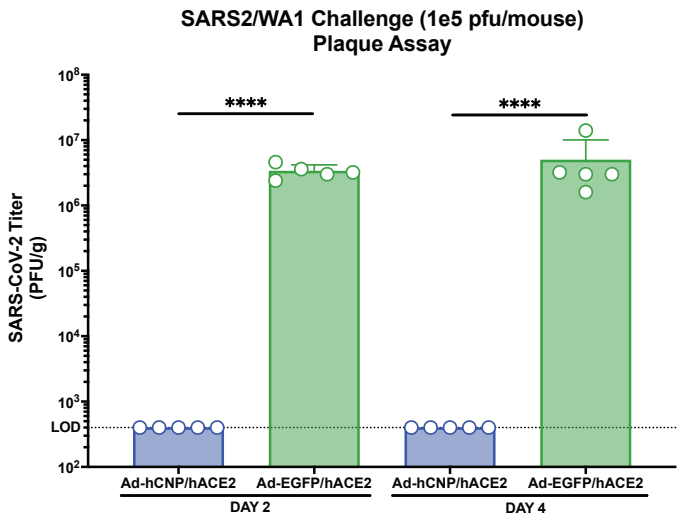

D

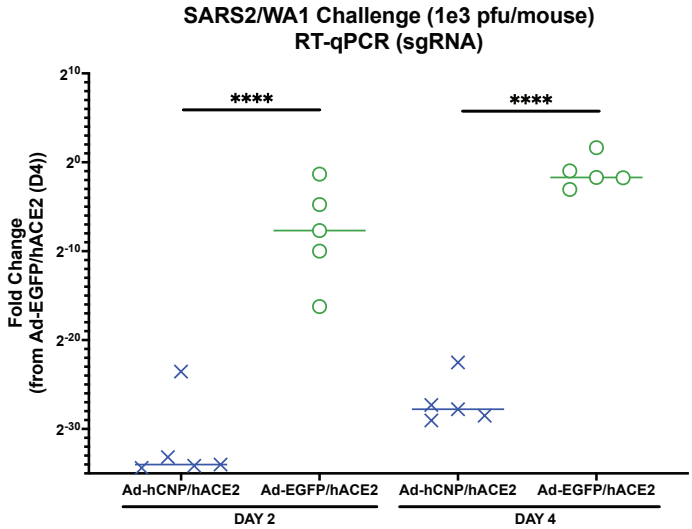

E

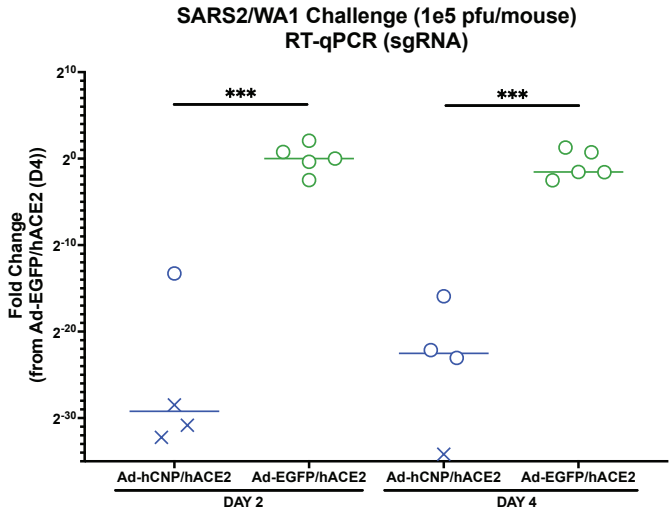

FIGURE S1

A

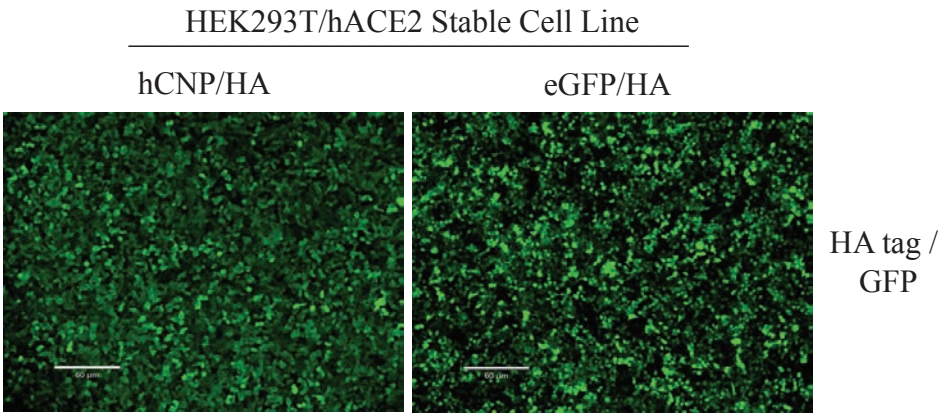
HEK293T/hACE2 Stable Cell Line
hCNP/HA
eGFP/HA
HA tag /
GFP

B

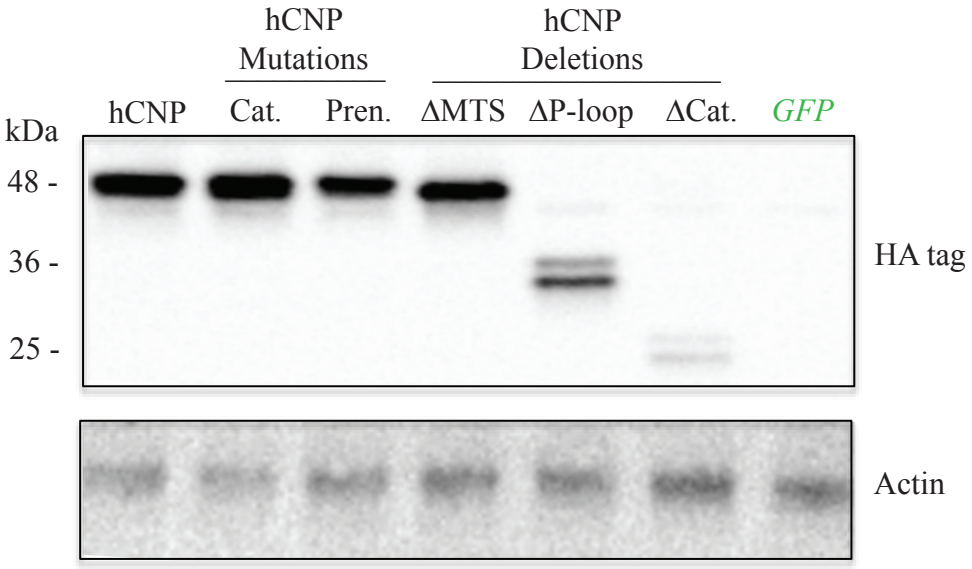
hCNP
Mutations
hCNP
Deletions
kDa
hCNP
Cat.
Pren.
ΔMTS
ΔP-loop
ΔCat.
GFP
48 -
36 -
25 -
HA tag
Actin

FIGURE S2

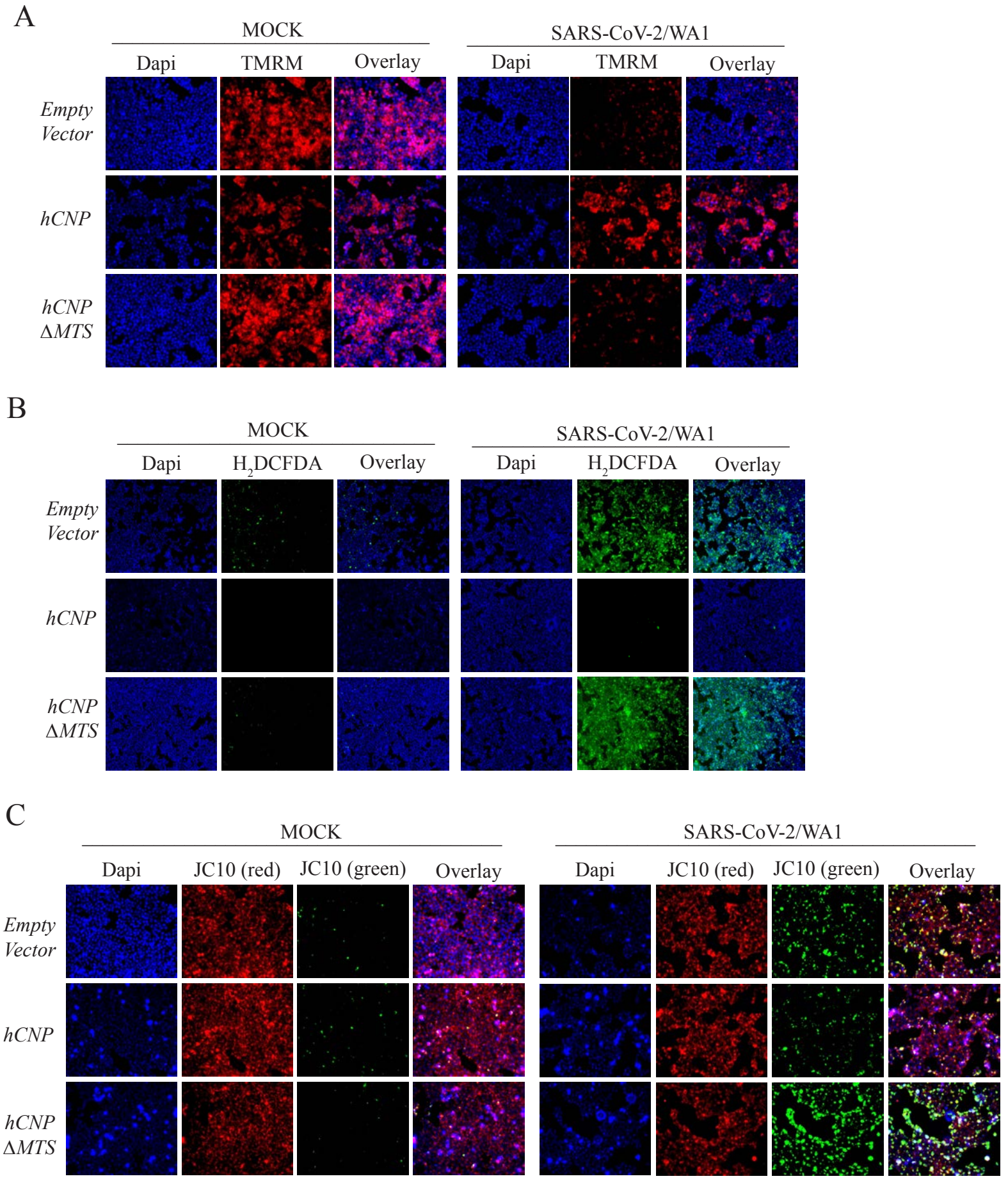
A
MOCK
SARS-CoV-2/WA1
Dapi
TMRM
Overlay
Dapi
TMRM
Overlay
Empty Vector
hCNP
hCNP ΔMTS
B
MOCK
SARS-CoV-2/WA1
Dapi
H2DCFDA
Overlay
Dapi
H2DCFDA
Overlay
Empty Vector
hCNP
hCNP ΔMTS
C
MOCK
SARS-CoV-2/WA1
Dapi
JC10 (red)
JC10 (green)
Overlay
Dapi
JC10 (red)
JC10 (green)
Overlay
Empty Vector
hCNP
hCNP ΔMTS